Stem Cell Reports
Article

ISSCR

OPEN ACCESS

In Vitro Differentiated Human Stem Cell-Derived Neurons Reproduce Synaptic Synchronicity Arising during Neurodevelopment

Filip Rosa,[1] Ashutosh Dhingra,[2] Betül Uysal,[1] G. Dulini C. Mendis,[3] Heidi Loeffler,[1] Gina Elsen,[1] Stephan Mueller,[1] Niklas Schwarz,[1] Melissa Castillo-Lizardo,[2] Claire Cuddy,[3] Felicitas Becker,[1] Peter Heutink,[2,4] Christopher A. Reid,[3] Steven Petrou,[3] Holger Lerche,[1,5,*] and Snezana Maljevic[1,3,5,*]

[1]Department of Neurology and Epileptology, Hertie Institute for Clinical Brain Research, University of Tuebingen, Tuebingen, Germany
[2]Genome Biology of Neurodegenerative Diseases, German Center for Neurodegenerative Diseases (DZNE), Tuebingen, Germany
[3]The Florey Institute for Neuroscience and Mental Health, The University of Melbourne, Melbourne, VIC, Australia
[4]Department for Neurodegenerative Diseases, Hertie Institute for Clinical Brain Research, University of Tuebingen, Tuebingen, Germany
[5]Co-senior author
*Correspondence: holger.lerche@uni-tuebingen.de (H.L.), snezana.maljevic@florey.edu.au (S.M.)
https://doi.org/10.1016/j.stemcr.2020.05.015

SUMMARY

Neurons differentiated from induced pluripotent stem cells (iPSCs) typically show regular spiking and synaptic activity but lack more complex network activity critical for brain development, such as periodic depolarizations including simultaneous involvement of glutamatergic and GABAergic neurotransmission. We generated human iPSC-derived neurons exhibiting spontaneous oscillatory activity after cultivation of up to 6 months, which resembles early oscillations observed in rodent neurons. This behavior was found in neurons generated using a more "native" embryoid body protocol, in contrast to a "fast" protocol based on NGN2 overexpression. A comparison with published data indicates that EB-derived neurons reach the maturity of neurons of the third trimester and NGN2-derived neurons of the second trimester of human gestation. Co-culturing NGN2-derived neurons with astrocytes only led to a partial compensation and did not reliably induce complex network activity. Our data will help selection of the appropriate iPSC differentiation assay to address specific questions related to neurodevelopmental disorders.

INTRODUCTION

Disease modeling using induced pluripotent stem cell (iPSC)-derived neurons is becoming an increasingly accepted alternative to studies of rodent models of neurogenetic disorders including epilepsy, autism, and schizophrenia (Tidball and Parent, 2016). Specific protocols for the generation of two- and three-dimensional neuronal cultures have been developed leading to a wide application of two major approaches in the modeling of brain disorders. One approach is a lengthy and sophisticated attempt to reach the most complex representation of *in vivo* processes by generating brain organoids (Bershteyn et al., 2017; Birey et al., 2017; Kadoshima et al., 2013; Lancaster et al., 2013; Mansour et al., 2018; Qian et al., 2016; Quadrato et al., 2017), while the second focuses on a fast production of homogeneous, stable neuronal populations using overexpression of specific transcription factors, most commonly Neurogenin 2 (NGN2) (Busskamp et al., 2014; Zhang et al., 2013).

In vivo neurodevelopment is a complex process starting in humans in the first trimester of pregnancy and continuing until adulthood. Following the initial step of neurulation that creates the neuroectoderm, different types of neural cells are made via asymmetric mitosis in a typical temporal order, from neurons to astrocytes and finally oligodendrocytes. The newborn cells migrate from a germinative zone to a terminal place and, after occupying it, connect to other cells. The first recorded neuronal activity is spontaneous firing, which is at a later stage driven by electric and eventually chemical synapses (Connors et al., 1983; Valiullina et al., 2016; Yu et al., 2012). Oscillatory neuronal activity, corresponding to a synchronous activity of neuronal assemblies, first develops mostly in projections from thalamus to the cortex. These initial, slow, intermittent oscillations are mediated by glutamatergic α-amino-3-hydroxy-5-methyl-4-isoxazolepropionic acid (AMPA) and *N*-methyl-D-aspartic acid (NMDA) receptors and appear around the 32nd week of gestation (Luhmann and Khazipov, 2018). They are replaced by faster continuous oscillations and desynchronization, caused by emerging intracortical connections and a maturing GABAergic system (Luhmann and Khazipov, 2018). The latter processes start after the 35th week of gestation and continue until infancy, with the prefrontal cortex reaching full maturity in humans at the age of 25 years (Vanhatalo and Kaila, 2006). Human and rodent neurodevelopment share common concepts but differ in fine details, such as thickness and layering of the cortex, emergence of an outer subventricular zone, and gyrification (Dehay et al., 2015; Testa-Silva et al., 2014). Human stem cell-based models may, therefore, provide novel insights into the developing human brain.

In this study, we used two alternative differentiation protocols. The first one is based on viral overexpression of the NGN2 transcription factor leading to the generation of

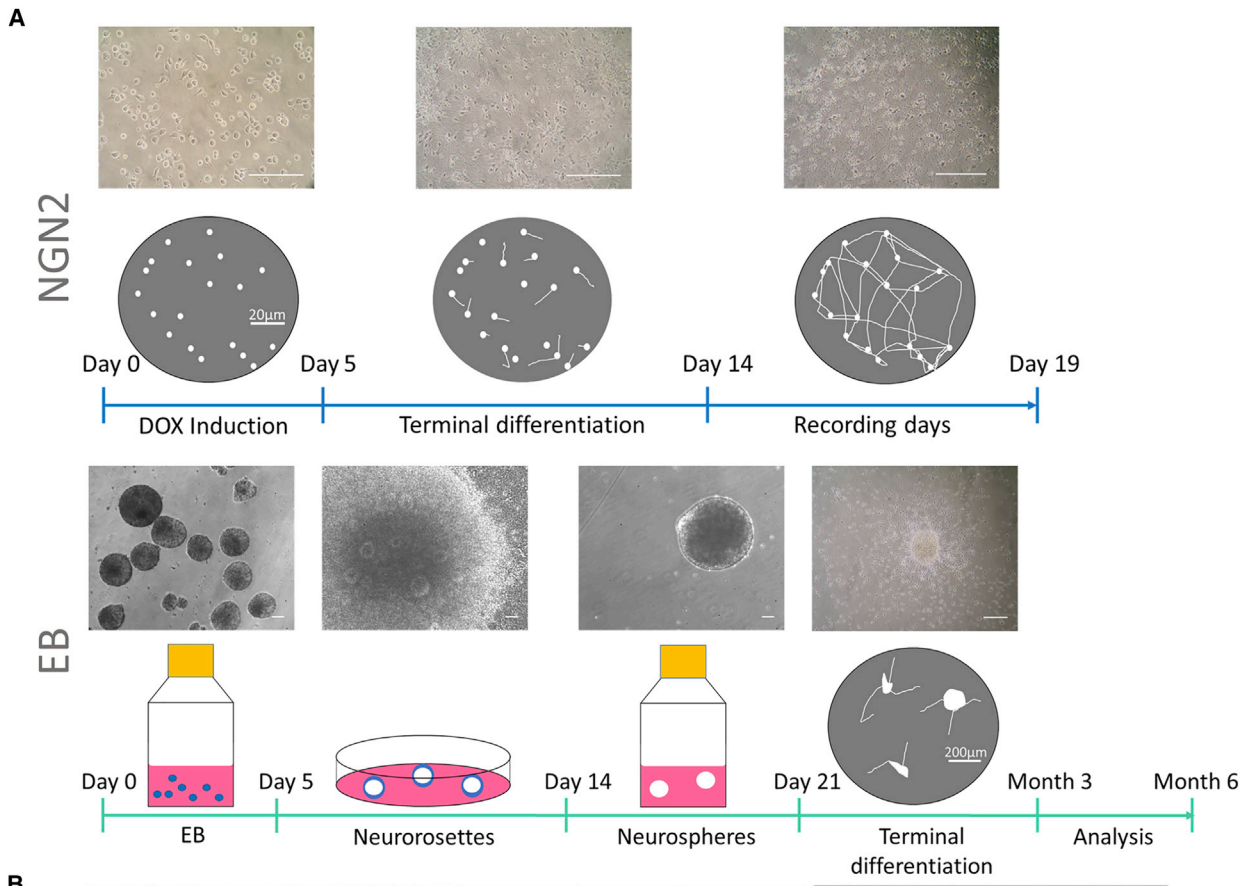

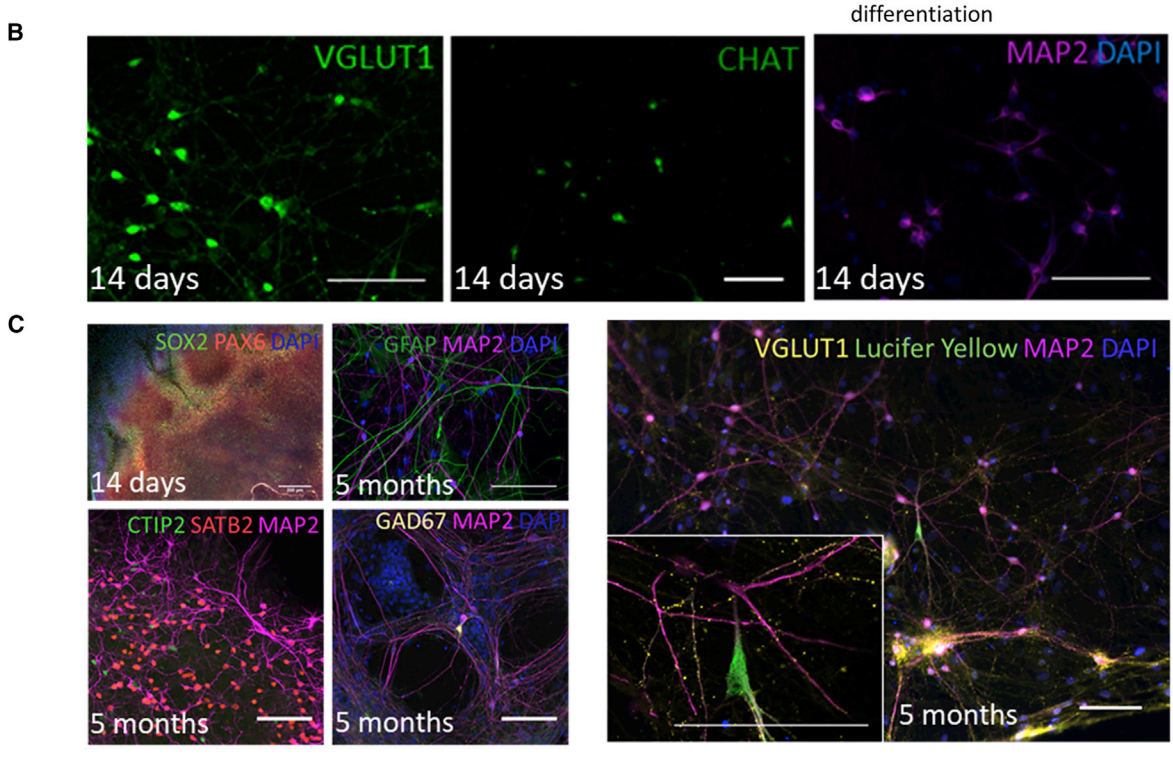

(legend on next page)

homogeneous glutamatergic active neuronal populations within 1–3 weeks of differentiation (Busskamp et al., 2014; Zhang et al., 2013). The second, embryoid body (EB)-based dual SMAD inhibition procedure uses a modified embryonic stem cell differentiation protocol (Chambers et al., 2009; Zhang et al., 2001) in an attempt to follow the natural path of neurogenesis. This protocol also results in the generation of glial cells (Kirkeby et al., 2012).

We aimed to (1) assess the ability of iPSC-derived neurons to generate a more complex and a more mature network activity important for neuronal development, and (2) test the two differentiation protocols in regard to maturity of generated neurons using a comparison with available data from human and rodent neurodevelopmental studies. Neurons generated by the NGN2 protocol were cultivated for 2–3 weeks and if co-cultured with murine astrocytes 6–7 weeks after the start of differentiation. Cultures derived using the EB protocol were matured for up to 6 months, which covers or exceeds the time points of analysis reported in the literature (Liu et al., 2013; Rubio et al., 2016; Sun et al., 2016). In contrast to other iPSC studies looking mostly at the RNA expression in different models to assess the identity and maturation of differentiated neurons, we focused on the assessment of electrophysiological properties that can provide a standardized concept across different species.

RESULTS

We used two protocols to differentiate iPSCs into cortical neuronal cultures (Figures 1A and S1). The first one, based on transgenic expression of NGN2 under doxycycline control (Busskamp et al., 2014; Zhang et al., 2013), produced pure neuronal cultures of regularly firing neurons starting from day 7 after induction (Lam et al., 2017). We characterized these neurons by dual immunostaining for the glutamatergic marker VGLUT1 and cholinergic marker CHAT on day 14. Both markers were expressed in the majority of generated neurons (Figure 1B; Busskamp et al., 2014). Patch-clamp recordings in these cultures were performed from day 14 to day 19 after induction. The second, EB-based protocol uses steps alternating between adhesive and floating growth with a timed addition and withdrawal of small molecules to recapitulate *in vivo* neurodevelopment. Electrophysiological recordings in these cultures were performed 3–6 months after the start of differentiation. Characterization of adhesive phases (neurorosettes and terminal neurodifferentiation) using immunostaining is shown in Figure 1C. Neural stem cell (NSC) markers, SOX2 and PAX6, were expressed in neurorosettes. Besides neurons (MAP2-positive cells), 5-month-old EB-derived cultures were enriched in astrocytes as indicated by the presence of glial fibrillary acidic protein (GFAP) staining (Figure 1C). We further found a prevailing number of cells expressing SATB2 (marking predominantly layers 2–4 cortical neurons) over CTIP2 (marking layer 5 projection neurons) in 4:1 ratio (n(SATB2) = 102, n(CTIP2) = 22). VGLUT1-positive glutamatergic neurons were present in a vast majority compared with GAD67-positive inhibitory cells (Figure S6), which accounted for less than 5% of all neurons (Figures 1C and S6). This corroborates the reports pointing at the necessity of a patterning factor, purmorphamine, for GABAergic neuronal differentiation (Liu et al., 2013; Sun et al., 2016; Yuan et al., 2015). We exclusively selected large pyramidal cells (Figure 1C, bottom) for patch-clamp recordings. From the start of terminal differentiation, both NGN2-derived and EB-derived neurons were kept in BrainPhys medium made in-house following the procedure described by Bardy et al. (2015).

Both differentiation protocols yielded electrophysiologically active cells (Figure 2A). Cells with a resting membrane potential (RMP) of −50 mV or below and firing more than one action potential were accepted for analysis. Evoked neuronal firing upon increasing current injections revealed early response of NGN2-derived neurons but a faster collapse of firing beyond current injections of 40 pA (Figures 2A and 2B). Older EB-derived neurons produced more action potentials at higher current injections (Figure 2A). To assess the maturity of cells, we used a ranking system that sorts stem cell-derived neurons into five types based on the overshooting amplitude of action potentials and the firing frequency (Bardy et al., 2015; see Supplemental Information). The analysis revealed that EB-derived neurons are more mature than NGN2-derived neurons, with less than 10% of recorded neurons not reaching type 5 maturity. For NGN2-derived neurons that proportion is 33% (Figure 2C).

There was no spontaneous synaptic activity detected in NGN2-derived cultures up to 19 days *in vitro*. In contrast, we recorded an abundant synaptic activity in EB-derived neurons, which was constantly improving during maturation of up to 6 months in culture (Figure 2D).

Figure 1. Neural Differentiation Protocols for Modeling of Cortical Pathologies

(A and B) (A) Timeline of the NGN2 protocol (top) and dual SMAD protocol (bottom). (B) Immunostainings of 14-day-old NGN2-differentiated neurons for VGLUT1, CHAT, and MAP2 protein expression.

(C) Immunostaining characterization of different stages of EB differentiation using specific antibodies. For rosettes (top left, day 14 of differentiation): SOX2 and PAX6; for 5-month-old EB cultures: GFAP and MAP2 (top right), CTIP2, SATB2, and MAP2 (bottom left), and GAD67 and MAP2 (bottom right). Right panel shows VGlut1and MAP2 staining, with a patched neuron filled with Lucifer yellow (inset). DAPI (blue) is used as a nuclear marker. Scale bars as stated in the image, otherwise 100 μm. See also Figures S1 and S6.

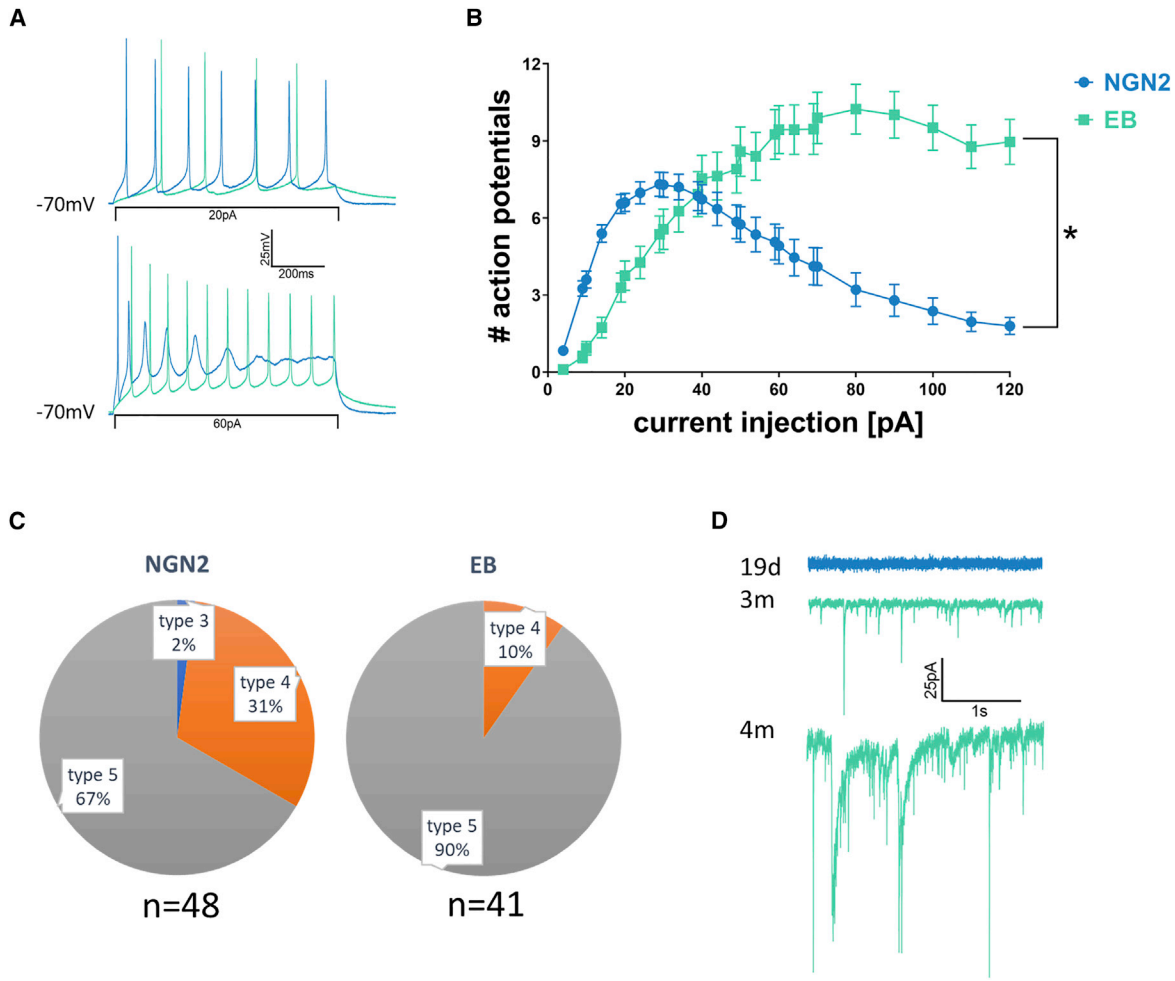

Figure 2. NGN2- and EB-Evoked and Synaptic Activity

(A) Representative action potential traces recorded from an NGN2 (blue) and an EB (green) neuron in response to 20 pA and 60 pA current stimulus applied for 800 ms. All cells were held at −70 mV.

(B) Input-output curves for 14- to 19-day-old NGN2 and 3- to 6-month-old EB neurons. *p = 0.0112 ($F_{1,87}$=6.716, n(NGN2) = 48, and n(EB) = 41 from three independent differentiations; two-way repeated-measurements ANOVA matched for cells, error bars indicate SEM).

(C) Diagrams showing distribution of neuronal maturity classes according to Bardy et al. (2016) (n(NGN2) = 48, n(EB) = 41).

(D) Representative traces of excitatory postsynaptic currents (EPSCs) recorded at −85 mV from 19-day-old NGN2 (blue) and 3-month-old (middle) and 4-month-old (bottom) EB cells (green). Only EB-derived neurons show spontaneous synaptic activity.

Oscillatory Activity in EB-Derived Neurons

Prolonged cultivation of EB-derived cells resulted in increased oscillatory activity. At 6 months, large pyramidal cells nested in a dense astrocytic population (Figures 1C [bottom] and 3A) showed oscillatory activity with intermittent low-frequency postsynaptic currents, which regularly reached amplitudes of ≥−500 pA and lasted for more than 1.5 s (mean ± SD: 4.39 ± 1.50 s) (Figure 3B, top panel). The frequency of events was one in 50 s (mean ± SD: 0.027 ± 0.024 Hz). Following 5-min recordings in the voltage-clamp mode, we regularly switched to the current-clamp mode and could detect events with the same frequency and duration (Figure 3B, bottom panel). We called these occurrences giant depolarization events (GDEs) and we retain this designation for both current-clamp and voltage-clamp recordings throughout the article. GDE duration and frequency as well as interburst interval were averaged for each recorded cell, and the distributions for all cells are shown in Figure 3C. More detailed characterization of the GDEs is described in Figures S2 and S3.

To identify the origin of GDEs, we performed a series of pharmacological experiments. Previous studies had reported an effect of the AMPA receptor blocker, cyanquixaline (CNQX), on fast excitatory postsynaptic currents (EPSCs) in stem cell-derived neurons (Espuny-Camacho et al., 2013; Lam et al., 2017). When we applied CNQX,

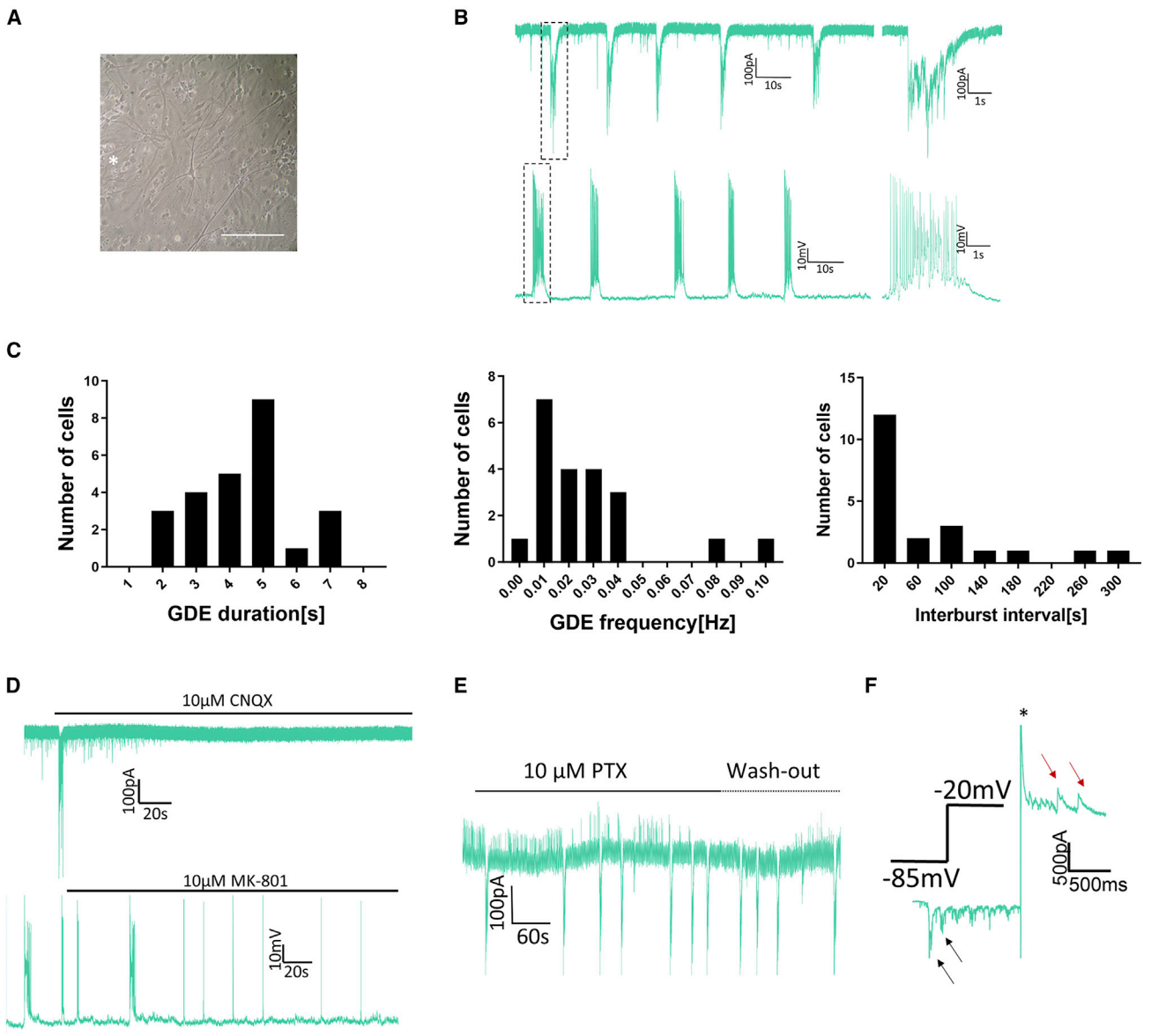

Figure 3. EB-Derived Neurons Present Giant Depolarization Events Resembling Spindle Bursts or Early Network Oscillations

(A) Bright-field image of a typical EB neuron (asterisk) showing giant depolarization events (GDEs). Scale bar, 100 μm.

(B) Representative trace of EPSCs organized in GDEs, recorded at −85 mV (top); spontaneous firing of the same cell recorded using a holding current of 0 pA (bottom). The areas marked with dashed rectangles are magnified on the right.

(C and D) (C) Left: frequency distribution of GDE duration, n(cells) = 25, bin width = 1 s; middle: frequency distribution of GDE frequency, n(cells) = 21, bin width = 0.01Hz; right: interburst interval, n(cells) = 21, bin width = 40 s. (D) Top: block of glutamatergic neurotransmission using AMPA blocker (holding potential −85 mV). Bottom: recordings in the current-clamp mode revealed that NMDA blocker MK-801 abolishes GDE bursts but not single spike firing. Holding current 0 pA.

(E) Voltage-clamp recording at −50 mV showing that PTX blocks IPSCs.

(F) Trace of a single GDE recorded at −85 mV and upon change of potential to −20 mV. The calculated chloride reversal potential was −85 mV, suggesting that downward events (black arrows) present EPSCs and upward events (red arrows) present IPSCs. Asterisk indicates capacitive and a potassium A-current.

The data were derived from three independent differentiations. See also Figures S2 and S3.

both fast EPSCs and GDEs were completely abolished (Figure 3D, top) with GDEs returning after washout (Figure S4A). In current-clamp recordings, we detected only action potentials evoked by current injections (data not shown). Application of the NMDA receptor blocker MK801 changed the firing pattern from GDE bursts to firing of single action potentials (Figure 3D, bottom). These data suggest a decisive glutamatergic drive for GDEs by both AMPA and NMDA receptors. Notably, this resembles the activity observed in *in vivo* recordings from the barrel cortex of neonatal rats (Minlebaev et al., 2009) and recordings in cortical slices (Garaschuk et al., 2000) extracted from rats of the same age, postnatal day 1 (P1) to P6 (Table S1). To assess the contribution of GABAergic activity, we performed voltage-clamp recordings at −50 mV, which enabled simultaneous recordings of EPSCs and inhibitory postsynaptic currents (IPSCs) (Figure 3E). Here, IPSCs appeared as upward events that could be blocked by 10 μM picrotoxin (PTX), a $GABA_A$ receptor blocker. After washout of PTX, IPSCs re-emerged (Figure 3E). The upward occurrence of IPSCs at this potential is in accordance with the calculated and measured chloride reversal potential at −85 mV (Figure S4B). The occurrence of IPSCs during GDEs stayed elusive due to massive AMPA receptor and NMDA receptor depolarizing currents. Therefore, we performed recordings whereby we changed the holding potential from −85 mV to −20 mV in the middle of a GDE (Figure 3F). This experiment showed clearly that EPSCs (downward currents at holding potential −85 mV) as well as IPSCs (upward currents at holding potential −20 mV) are simultaneously present in GDEs.

Application of 10 μM PTX blocked outwardly displayed IPSCs but also induced large inward currents corresponding to GDEs recorded in current-clamp mode (Figure 3E). To further examine the role of GABAergic transmission in the generation of GDEs, we applied 10 μM PTX in current-clamp recordings (Figure 4A). Upon application of PTX, the firing pattern changed from frequent single spikes with only rare transient depolarizations with bursts of action potentials to a pure pattern of depolarizing bursts. Further analysis revealed that inhibitory postsynaptic potentials (IPSPs) caused a sag in membrane potential before PTX application, followed by an increased action potential overshoot presumably due to a restoration of a portion of inactivated sodium channels (Rama et al., 2015). This was not seen in recordings with PTX. The average increase of the action potential overshoot of the five events marked by arrows in Figure 4A was 9.86 ± 2.25 mV; for the events recorded in the presence of PTX, the averaged overshoot increase was 0.38 ± 0.99 mV ($p = 0.0095$ using Welch's t test). A similar effect was observed when firing was evoked by current injections. In this case, a preceding IPSP could increase the overshoot of an immediately following action potential (Figure S4C).

Several of 25 recorded cells exhibiting GDEs achieved an interplay of EPSCs and IPSCs with an oscillatory pattern. Figure 4B depicts two most developed oscillations we recorded that resembled a delta oscillation, on the left, and a theta oscillation, on the right. The cell showing delta oscillations is driven by EPSCs (black arrows), recorded at the holding potential of −85 mV. Voltage-clamp recording at the holding potential of −50 mV in the cell showing theta oscillatory pattern suggests the involvement of both EPSCs (black arrows) and IPSCs (red arrows), resulting in a faster oscillatory pattern than seen in the cell showing the delta oscillation. A summary of the changes in synaptic and oscillatory activity during the development in culture is shown in Figure 4C.

To test whether the development of GDEs is correlated with maturation of the GABAergic system, we investigated the expression of the transporters *NKCC1* and *KCC2* involved in regulation of neuronal chloride homeostasis and in the so-called GABA switch during neuronal development were investigated (Khirug et al., 2005; Rivera et al., 1999). We also studied *SCN1A* as the major sodium channel of inhibitory neurons (Yu et al., 2006; Ogiwara et al., 2007) in 2- and 6-month-old EB-derived cultures. The experiments were designed as an absolute quantification, enabling us to calculate the ratio of *NKCC1*/*KCC2* for each sample. For *SCN1A* analysis, we normalized the quantity of *SCN1A* to *MAP2* to control for the different proportions of non-neuronal cells in the bulk isolation of RNA. No changes were found in the *NKCC1*/*KCC2* ratio during 4 months of maturation (Figure 4D, mean ± SEM, 2 months: 12 ± 9.32; 6 months: 8.53 ± 3.56; $p = 0.486$). *SCN1A* expression normalized to *MAP2* showed an upregulation within the same period (Figure 4D; mean ± SEM, 2 months: 0.035 ± 0.013; 6 months: 0.148 ± 0.043; after square-root transformation, 2 months: 0.168 ± 0.049; 6 months: 0.371 ± 0.057; $p = 0.0358$—the square-root transformation was used to achieve a normal distribution in order to apply a t test).

Functional Properties and Neural Cell Growth

Cell capacitance, indicating the size of the recorded neurons, was proposed as a better marker of maturation than the time from the start of neuroinduction (Bardy et al., 2016) (Figure S5A). After observing a strong correlation of GDE duration with cell capacitance ($r = 0.488$, $p = 0.0132$) (Figure 5A), we explored whether passive neuronal properties could explain the functional differences between NGN2-derived and EB-derived cells. Both capacitance (mean ± SEM, NGN2: 22 ± 1 pF; EB: 70 ± 6 pF; $p < 0.0001$) and input resistance (mean ± SEM, NGN2: 1,908 ± 132 MΩ; EB: 441 ± 56 MΩ; $p < 0.0001$) were significantly different (Figures 5B and 5C). When we compared input resistances with reported values from recordings in human brain tissue during the second trimester

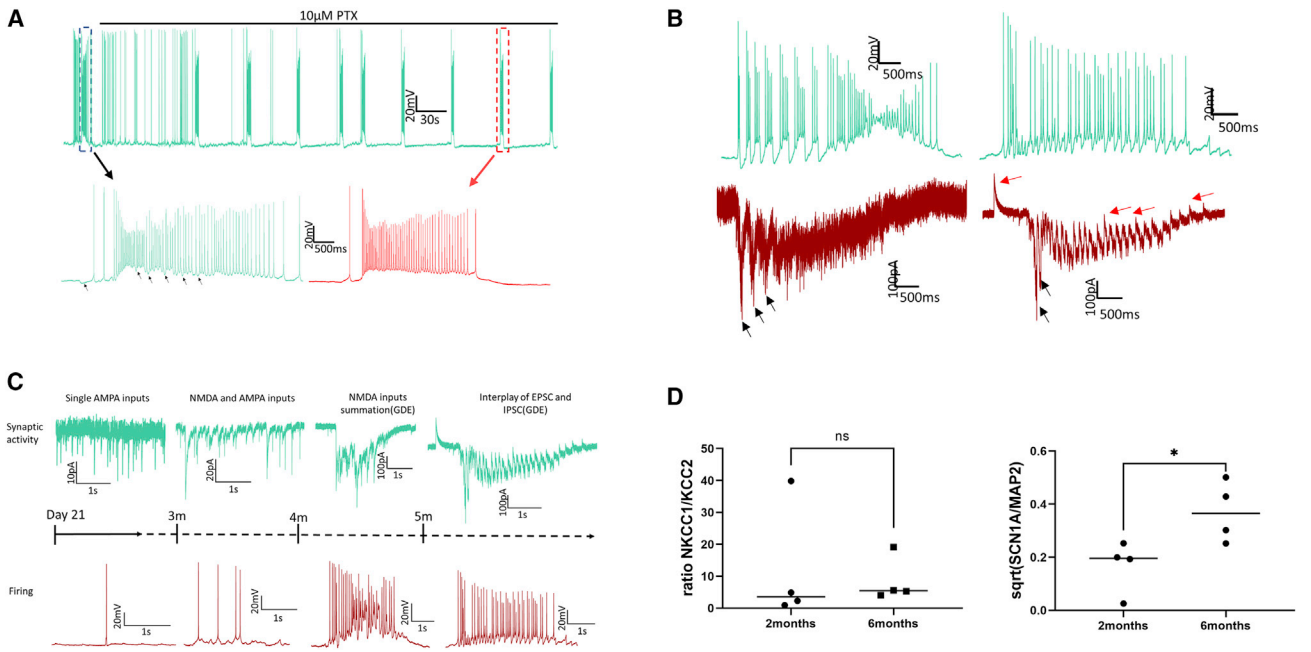

Figure 4. Characteristics and Development of GDEs

(A) Top: firing activity (holding current 0 pA) before and after application of $GABA_A$ blocker PTX. Bottom: magnified views show presence of IPSPs before PTX application (black arrows, left) and their block after application (right).

(B) Top left: recorded trace of a delta frequency oscillation. An extract from current-clamp recording of a 5-month-old neuron, holding current 0 pA during recording. Bottom left: corresponding voltage-clamp recording from the same cell at the holding potential of −85 mV. Top right: recorded trace of theta frequency oscillation. An extract from current-clamp recording of a 5-month-old neuron, holding current 0 pA during recording. Bottom right: corresponding voltage-clamp recording from the holding potential of −50 mV to display both IPSCs and EPSCs.

(C) Chronological development of synchronized activity in EB-derived neurons. Green traces: synaptic activity recorded in voltage-clamp mode; red traces: corresponding firing recorded in current-clamp mode with I_h= 0 pA. Voltage-clamp and current-clamp traces were obtained from the same cell of the particular age. During development in culture, the activity changes from single AMPA events later enriched by NMDA events to GDEs. Addition of hyperpolarizing GABA events enables faster and prolonged oscillations.

(D) Left: scatterplot of expression analysis of *NKCC1* and *KCC2* transporters plotted as an *NKCC1/KCC2* ratio (p = 0.4857, n(2 months) = 4, n(6 months) = 4, Mann-Whitney test, U = 5). Right: scatterplot of expression analysis of *SCN1A* normalized to *MAP2* plotted as a ratio of both genes after square-root transformation (*p = 0.0358, n(2 months) = 4, n(6 months) = 4, unpaired t test).

See also Figures S2–S4.

(Moore et al., 2009) and in adult human neurons (Testa-Silva et al., 2014), we found that approximately half of the NGN2-derived neurons had input resistances similar to those of the second trimester brain tissue, whereas EB-derived cells were closer to adult human neurons (Figure 5C). A hyperbolic function was fit to the capacitance-input resistance relationship for all recorded cells (Figure 5D):

$$R_{\text{in}} = \frac{2.09E^6}{\left(C^2 + 743.2\right)} \sim \frac{r_{\text{m}}}{A} = \frac{r_{\text{m}}}{4\pi r * r} = \frac{r_{\text{m}}}{4\pi r^2} = \frac{x}{r^2} = \frac{\Delta U}{\Delta I},$$

where R_{in} is input resistance, C is capacitance, r_{m} is specific membrane resistance, A is area, r is radius, $x = \frac{r_{\text{m}}}{4\pi}$, ΔU is voltage deviation, ΔI is current injection, and R^2= 0.4866. Since the size of the cell determines input resistance, the relationship represents a hyperbolic decline of input resistance in growing neurons starting from the same capacitance of 15 pF recorded in iPSCs before the start of differentiation (data not shown).

To assess the impact of cell growth on firing properties (Figure 2B), we recalculated the input-output curve of NGN2-derived neurons using the input resistance recorded in EB-derived neurons using the following formula:

$$\text{Current to inject}_{\text{recalculated}} = \text{Current to inject}_{\text{NGN2}} \times \frac{R_{\text{in}}^{\text{NGN2}}}{R_{\text{in}}^{\text{EB}}}.$$

Figure 5E shows the result of this simple calculation indicating that the NGN2-derived neurons' input-output curve more closely resembled the one obtained for EB-derived neurons with a deviation at lower current stimulations. EB-derived cells had significantly lower RMP (Figure 5F; mean ± SEM, NGN2: −58.8 ± 0.9 mV;

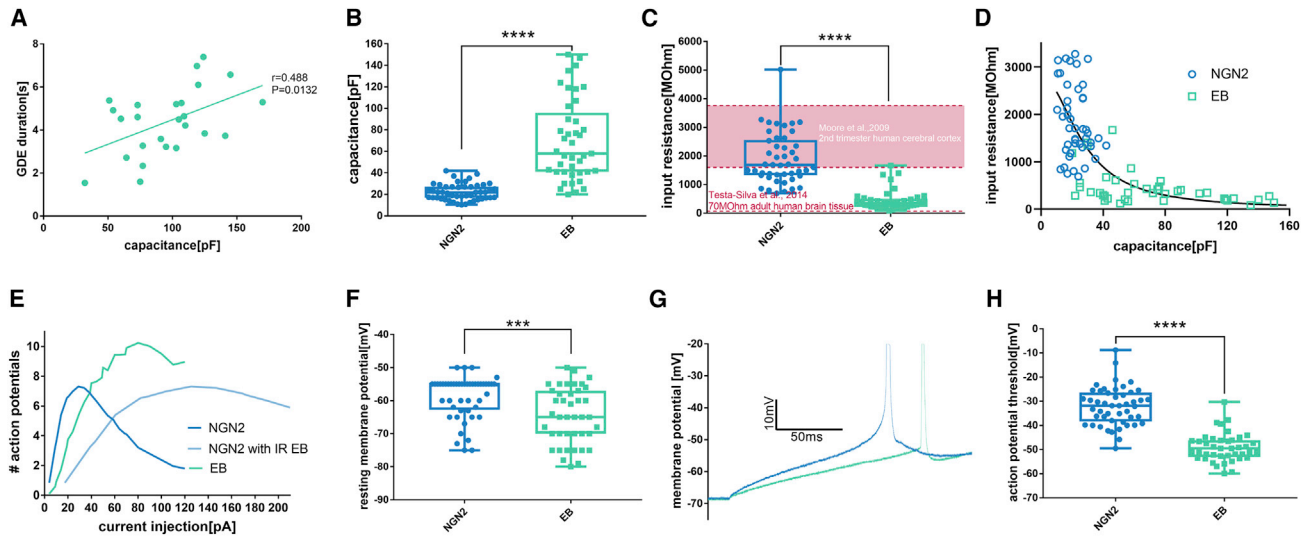

Figure 5. Cell Growth and Electric Properties of Differentiated Neurons

(A) Correlation of cell capacitance and GDE duration in EB neurons. Pearson's r = 0.488, p = 0.0132, n = 25, R^2 = 0.2385.

(B) Boxplot of cell capacitance values for NGN2-derived versus EB-derived neurons. ****p < 0.0001, n(NGN2) = 48, n(EB) = 41, Welch's t = 7.962.

(C) Boxplot of input resistance values for NGN2-derived versus EB-derived neurons. ****p < 0.0001, n(NGN2) = 46, n(EB) = 41, Mann-Whitney test U = 65. The red field marks a range of input resistance recorded by Moore et al. (2009) in the human fetal brain tissue aborted in the second trimester. The red dashed line marks a mean input resistance in human adult cortical tissue recorded by Testa-Silva et al. (2014).

(D) Non-linear fit of input resistance relation to capacitance for all recorded NGN2-derived and EB-derived neurons; n(NGN2 + EB) = 46 + 41 = 87, R^2 = 0.4866.

(E) Averaged input-output curves from Figure 2B with additional NGN2 curve recalculated for input resistance (IR, R_{in}) of EB-derived neurons.

(F) Boxplot of resting membrane potentials of NGN2-derive versus EB-derived neurons. ***p = 0.0004, n(NGN2) = 48, n(EB) = 41, Mann-Whitney test U = 568.

(G) Representative traces of the first action potential emerging in recordings from an NGN2-derived and EB-derived neurons upon current injection.

(H) Boxplot of action potential threshold values of NGN2-derived versus EB-derived neurons determined at 20 V/s. ****p < 0.0001, n(NGN2) = 48, n(EB) = 41, Mann-Whitney test U = 84.

Color coding: NGN2, blue; EB, green. Data were derived from three independent differentiations. ***p < 0.001; ****p < 0.0001. See also Figure S5. Boxes indicate 25–75 percentil of data distribution and whiskers indicate range.

EB: −64.6 ± 1.3 mV; p = 0.0004) and action potential threshold (Figures 5G and 5H; mean ± SEM, NGN2: −32.1 ± 1.1 mV; EB: −49.2 ± 0.92 mV; p < 0.0001). Hence, we analyzed the voltage that evoked the maximum sodium current for both NGN2-derived and EB-derived neurons and found that in NGN2-derived neurons this voltage was more depolarized (Figures S4D and S4E; mean ± SEM, NGN2: −24.2 ± 1.8 mV; EB: −47.8 ± 1.5 mV; p < 0.0001), suggesting that a different pool of sodium channels may underlie firing in the two neuronal populations.

NGN2-Derived and EB-Derived Neurons Have Divergent Fates from the Start of Differentiation

We also examined the correlation of action potential threshold with cell capacitance. Whereas NGN2-derived cells showed no correlation (r = 0.02, p = 0.890), for EB-derived neurons we observed a bisegmental linear relationship with a breakpoint at 49 pF (r = 0.59, p = 0.016) (Figure 6A and 6B; zoomed-in area 0–49 pF). As the properties of sodium channels are an important determinant of the action potential threshold, expression levels of three major alpha sodium channel subunits expressed in the brain were determined using qRT-PCR. The analysis was performed for each of the protocols at the stage of differentiation corresponding to the electrophysiological experiments. In NGN2-derived neurons, *SCN3A* was the most abundantly expressed sodium channel, followed by *SCN2A* and *SCN8A*. In contrast, *SCN2A* channels were the most abundant in EB-derived neurons (Figure 6C).

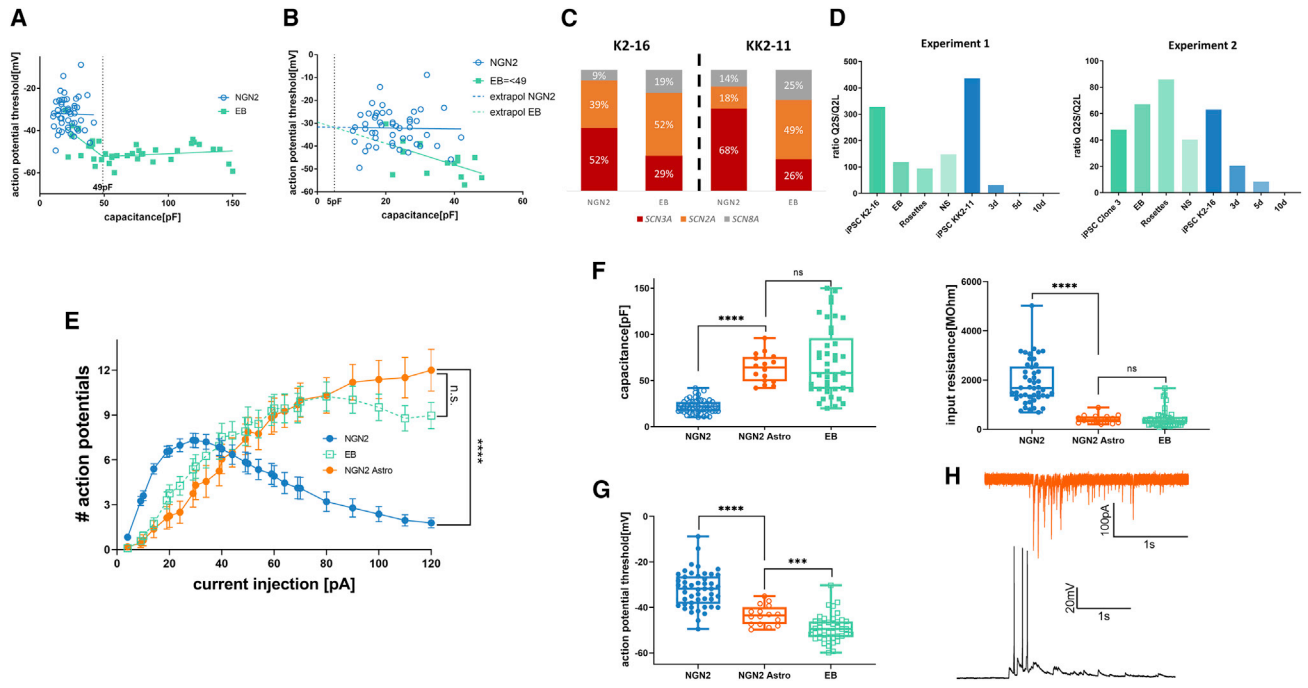

Figure 6. NGN2 and EB Neurons Have Different Expression Profiles

(A) Segmental linear regression with x_0= 49 pF. NGN2: $y = -31.64 - 0.0201x$, n(NGN2) = 48. EB:$y_1 = -29.49 - 0.4665x$ after x_0:$y_2 = -52.3485 + 0.0268(x - x_0)$, $R^2 = 0.3936$, n(EB) = 41.

(B and C) (B) Magnified plot of (A) in a range up to 49 pF. NGN2: Pearson's r = 0.02, p = 0.890, $R^2 = 0.0003$. EB: Pearson's r = 0.59, p = 0.016 $R^2 = 0.3513$. (C) Ratios of expression of three major sodium channels in two NGN2 and two EB lines determined by qRT-PCR.

(D) Ratio of expression of a short *KCNQ2* transcript versus long *KCNQ2* transcript determined in two independent qRT-PCR experiments.

(E) Input-output curves for 14- to 19-day-old NGN2, 3- to 6-month-old EB, and 7-week-old NGN2 neurons co-cultured with astrocytes (NGN2 Astro). *p = 0.0288 ($F_{2,102}$=3.672, n(NGN2) = 48, n(EB) = 41 from three independent differentiations and n(NGN2 Astro) = 16 from five independent differentiations); two-way repeated-measurements ANOVA matched for cells. Tukey's multiple comparison test: p(NGN2 versus EB) < 0.0001, p(NGN2 versus NGN2 Astro) < 0.0001, p(EB versus NGN2 Astro) = 0.6283. The error bars indicate SEM.

(F) Left: boxplot of cell capacitance values for NGN2-derived versus EB-derived versus NGN2 Astro neurons. ****p < 0.0001, n(NGN2) = 48, n(EB) = 41, n(NGN2 Astro) = 16, Kruskal-Wallis test. Dunn's multiple comparison test: p(NGN2 versus EB) < 0.0001, p(NGN2 versus NGN2 Astro) < 0.0001, p(EB versus NGN2 Astro) > 0.9999. Right: boxplot of input resistance values for NGN2-derived versus EB-derived versus NGN2 Astro neurons. ****p < 0.0001, n(NGN2) = 48, n(EB) = 41, n(NGN2 Astro) = 16, Kruskal-Wallis test. Dunn's multiple comparison test: p(NGN2 versus EB) < 0.0001, p(NGN2 versus NGN2 Astro) < 0.0001, p(EB versus NGN2 Astro) > 0.9999.

(G) Boxplot of action potential threshold values for NGN2-derived versus EB-derived versus NGN2 Astro neurons. ****p < 0.0001, n(NGN2) = 48, n(EB) = 41, n(NGN2 Astro) = 16, ANOVA test. Dunnett's multiple comparison test: p(NGN2 versus EB) < 0.0001, p(NGN2 versus NGN2 Astro) < 0.0001, p(EB versus NGN2 Astro) = 0.0009.

(H) Top: the only trace of EPSCs organized in immature form of GDE, recorded at −85 mV in one of 16 analyzed neurons. Bottom: spontaneous firing of the same cell recorded using a holding current of 0 pA.

Color coding: NGN2, blue: EB, green: NGN2 Astro, orange. See also Figure S6. Boxes indicate 25–75 percentil of data distribution and whiskers indicate range.

We further assessed expression levels of different transcripts of another ion channel. *KCNQ2* has several different isoforms, with the short one shown to be expressed only early in development (Smith et al., 2001). For these experiments, we performed an absolute quantification yielding the number of copies in 10 ng of whole RNA and divided the quantity of the short transcripts (Q2S) by the quantity of the long transcripts (Q2L). Our analysis revealed that the short variant is abundantly expressed at different stages of EB differentiation, but NGN2-derived neurons fail to express it at high levels (Figure 6D and Table S2).

As a next step, we co-cultivated NGN2-derived neurons with murine astrocytes to test whether their addition can improve the firing and network properties of NGN2-derived cultures toward those observed for EB-derived neurons (Figure S6). Indeed, the co-cultivated neurons were viable for up to 8 weeks, at which point the cultures started to decline. Thus, we analyzed 6- to 7-week-old cells, which

appeared similar to EB-derived neurons with regard to evoked firing as well as to their capacitance and input resistance (Figures 6E and 6F). However, the co-cultivated NGN2-derived neurons showed an only partially hyperpolarized action potential threshold and did not reach the action potential threshold of EB-derived neurons (Figure 6G). Furthermore, we could not detect higher network activity like the GDEs observed for EB-derived neurons, except for one from 16 recorded cells displayed in Figure 6F. In contrast to GDEs recorded from EB-derived neurons (Figures 3 and 4), no clear summation of NMDA inputs was seen in these recordings; we also did not detect IPSP events in these neurons, which is in line with the absence of interneurons in our NGN2-derived cultures (Figure S6C) (Zhang et al., 2013).

DISCUSSION

We showed that iPSC-derived neurons cultured with a classical EB protocol for 6 months develop oscillatory activity resembling the activity known from the developing rodent brain, which has also been correlated with electroencephalographic recordings in humans (Dupont et al., 2006; Luhmann and Khazipov, 2018; Vanhatalo et al., 2002). This activity was not detectable following a fast differentiation using the NGN2 protocol without astrocytes, and only one cell from NGN2-derived cultures co-cultivated with astrocytes showed a network activity somewhat different to the GDEs observed in EB-derived neurons. We further used electrophysiological parameters to estimate the correlations with gestational age and showed that EB-derived neurons reach a more advanced grade of maturity compared with NGN2-derived neurons. This was also corroborated by the expression patterns of major sodium channel genes. Furthermore, the expression of two different splice variants of the *KCNQ2* potassium channel supported our anticipation that NGN2-derived cells do not follow a typical path of neurogenesis from the start of differentiation.

Nature and Properties of GDEs

Recordings in EB-derived neurons differentiated for at least 4 months revealed spontaneous oscillatory activity, which we named GDEs. Two other studies reported a similar activity in human iPSC-derived neurons, but only after pharmacological induction (Pruunsild et al., 2017; Zhong et al., 2017). The observed GDEs are driven by massive depolarizing currents, which regularly result in a depolarization block (Figures 3B [bottom] and S3B [bottom]). In voltage-clamp recordings of GDEs, we recognized two different excitatory events, fast (10–100 Hz) and slow (0.05–5 Hz). Recordings in the presence of CNQX revealed that the fast inputs are AMPA receptor mediated. Application of the NMDA receptor blocker MK801 suggested that the slow inputs are mediated by NMDA receptors as previously reported in the literature (Garaschuk et al., 2000; Minlebaev et al., 2009). Due to their slow kinetics (Minlebaev et al., 2009), NMDA receptor inputs can be summed up as leading to the occurrence of GDEs (Figure 4C). Since our recordings showed that all activity could be blocked by CNQX, AMPA events must appear before NMDA events. This makes sense from the physiological perspective, as the depolarization caused by AMPA receptor activation is needed to remove the Mg^{2+} block of NMDA receptors (Leinekugel et al., 1997).

The periodic activity of GDEs shown in Figures 3 and 4 in both current-clamp and voltage-clamp mode, together with the predominant glutamatergic mechanism, suggests a resemblance to spindle bursts observed in recordings from P1–P6 rat cortex (Minlebaev et al., 2009). Spindle bursts, which are generally accepted as the analogous activity to a delta-brush recorded in human preterm newborn EEG, are proposed to synchronize the activity of local neuronal networks and affect corticogenesis (Luhmann and Khazipov, 2018). Consistent with this, a recording from a cell that was presumably among the most developed ones showed oscillations in the delta frequency band (Figure 4B, left). A selection of similar developmental events is displayed in Table S1. Giant depolarization potentials (GDPs) represent another type of oscillatory developmental event. GDPs have been recorded in hippocampal slices in rats at P1–P8 and are driven by GABAergic depolarizations (Ben-Ari et al., 1989). However, our data suggest that the glutamatergic drive is critical for the initiation of GDEs while the main role of GABA is their maintenance by providing restoration from depolarization block at the plateau phase (Figures 4A, 4B, S3B, and S4C). This behavior enables oscillations with a prolongation of GDEs. A recent study reported similar findings using analysis of at least 6-month-old iPSC-derived organoids with multielectrode arrays (Trujillo et al., 2019).

One limitation of our work is that we could not assess the potential depolarizing action of GABA (Kirmse et al., 2015), since we used whole-cell and not perforated patch-clamp recordings. We may have therefore biased the chloride reversal potential toward inhibition. However, GABA inputs were mostly active during GDEs. If they were depolarizing, they would present an additional depolarizing drive besides AMPA and NMDA currents, which would rather prevent oscillations and therefore not make sense in a physiological context. We examined the expression of two genes responsible for the so-called GABA switch in EB-derived cultures but did not find any significant difference between 2- and 6-month-old cultures. Interestingly, *SCN1A* expression increased in the same period. Although

we could not confirm whether this was limited to its expression in inhibitory neurons, it goes along with the observation of an increased contribution of inhibitory activity to GDEs recorded from older neurons.

Developmental Changes of Neuronal Properties and Gene Expression in Adjustment to Cell Growth

Since GDE duration was positively correlated with cell capacitance (Figure 5A), we investigated the correlation of passive membrane properties with the cell behavior. The development of a neuron is tightly correlated with its growth, since axonal and dendritic sprouting is essential to connect with other neurons at increasing distances within the growing networks. However, growth alone would cause a hyperbolic decline of input resistance, leading to an increased threshold for synaptic inputs to induce an action potential. This is further complicated by an increasingly hyperpolarized RMP, presumably due to an increased expression of different proteins, such as K^+ channels and Na^+/K^+ ATPase (Biser et al., 2000; Watari et al., 2013). This unfavorable fate of a growing neuron is illustrated in Figure 5E, which shows that NGN2-derived neurons with an input resistance of EB-derived neurons would become insensitive to low current stimulations. However, although EB-derived neurons have a more than 4-fold lower input resistance and more hyperpolarized RMP compared with 2-week-old NGN2-derived neurons, they still possess a sufficient excitability at low current stimulations to generate action potentials. In EB-derived neurons, the potential loss of excitability at low current stimulations is counteracted by a shift of the action potential threshold (Figures 5G, 5H, and S6). Our qRT-PCR experiments looking at the expression of three main excitatory neuronal sodium channels ($Na_V1.2$, $Na_V1.3$, and $Na_V1.6$ encoded by the genes *SCN2A*, *SCN3A*, and *SCN8A*, respectively) revealed higher relative expressions of *SCN2A* and *SCN8A* in EB-derived than in NGN2-derived neurons. In previous studies, $Na_V1.6$ channels have been especially associated with a hyperpolarizing shift of the action potential threshold (Royeck et al., 2008; Rush et al., 2005; Tadros et al., 2015). Without this shift in action potential threshold, maturing neurons would probably not be able to fire upon small synaptic inputs.

Interestingly, a bilinear fit with a breakpoint at 49 pF yielded the best result to describe the relationship between the action potential threshold and the cell capacitance (which we used as a measure of maturity) for EB-derived neurons (Figure 6A). The action potential threshold was continuously hyperpolarized until a capacitance of almost 50 pF was reached and then remained stable. In contrast, there was no correlation between cell capacitance and action potential threshold in NGN2-derived neurons (Figures 6A and 6B).

In addition to the different expression profiles of sodium channels, a voltage-gated *KCNQ2* channel showed a largely distinct developmental expression: the short transcript of *KCNQ2* is abundantly expressed in EB-derived differentiating cells but is instantly downregulated during differentiation of iPSCs into NGN2-derived neurons.

Other fundamental differences in the two differentiation protocols may account for the distinct maturity of differentiated neurons. During the first 21 days of the EB protocol, cells still divide and differentiate from iPSCs into common neural precursor cells, as is known from *in vivo* data (Geschwind and Rakic, 2013). EB-derived neurons then also migrate out of EBs. In the NGN2 protocol, neurons are differentiated directly from iPSCs and there is no migration in the culture dish. The combined approach with addition of the SMAD and WNT inhibitors (Nehme et al., 2018) in the first days of NGN2 differentiation can overcome some of the discordances between the protocols.

The addition of astrocytes proved to be an effective technical way to improve maturity of NGN2-derived neurons showing larger capacitance and smaller input resistance and allowed formation of functional synapses (Figure 6). However, a declining number of neurons during culturing due to the lack of progenitor cells and the absence of interneurons (Zhang et al., 2013), in addition to the depolarized action potential threshold and the undeveloped complex network activity such as GDEs, set limitations to the use of NGN2-derived neurons with or without astrocytes as developmental disease models.

Estimating Gestational Maturity of iPSC-Derived Neurons

The mature EB-derived neurons showed spontaneous activity similar to neurons at P1–P6 from rat neocortex *in vivo*, suggesting that GDEs potentially show a correlation with spindle bursts and, hence, to delta-brushes. This analogy indicates that the gestational age of EB-derived cells lies within the last trimester of pregnancy in humans (Luhmann and Khazipov, 2018; Vanhatalo and Kaila, 2006). These results also nicely fit with transcriptomic studies concluding that the best developed human iPSC neuronal cultures can rarely reach late fetal maturity (Stein et al., 2014). The input resistance of the EB-derived cells was close to that described in human adult brain neurons (70 MΩ) (Testa-Silva et al., 2014). This is in accordance with our data showing that the input resistance has a hyperbolic relationship with the cell growth (Figure 5D). In contrast to the EB protocol, the NGN2 protocol generated reliably firing cells within 2–3 weeks with input resistances corresponding approximately to the second trimester; this considerably less mature stage of development was also reflected in the different gene expression profiles discussed above. The 6- to 7-week-old

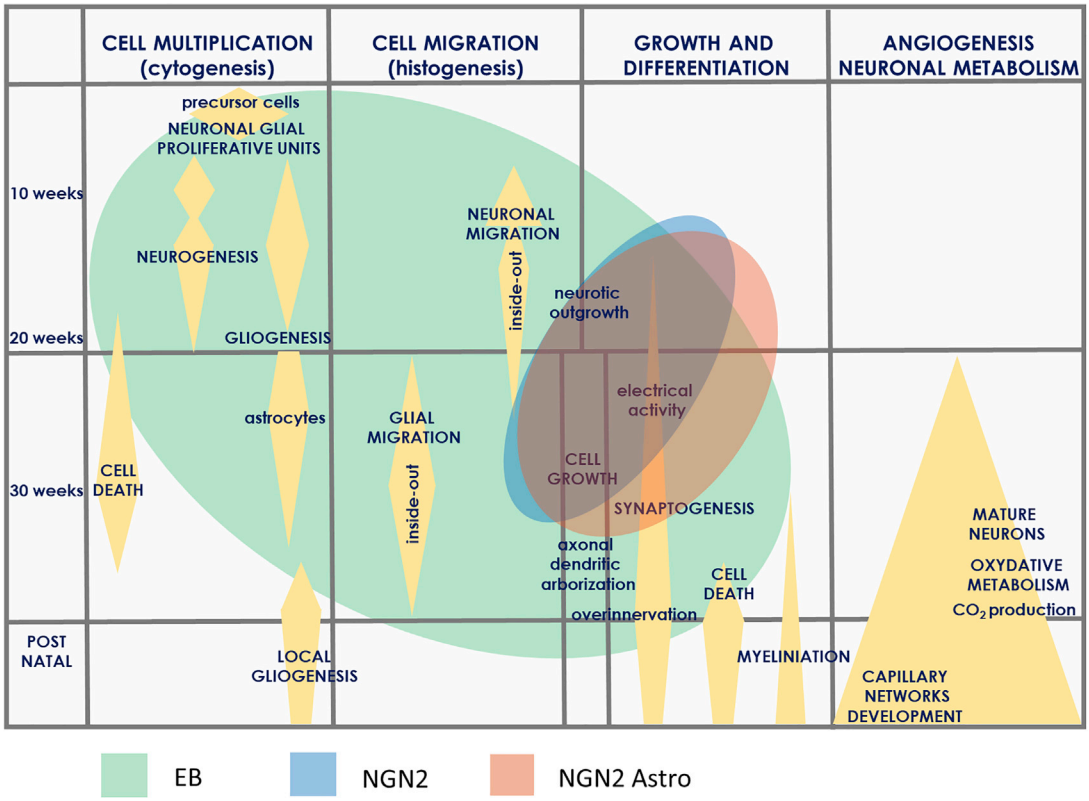

Figure 7. Schematic of the *In Utero* Neurodevelopmental Processes in Human

The simplified graph shows a timeline for major events of neural development that occur during prenatal and postnatal periods, and the developmental processes we suggest are covered by two differentiation protocols used in this study. Blue, NGN2 protocol; green, EB protocol. Modified after Ervard et al. (1996).

NGN2-derived neurons co-cultured with astrocytes reached the third trimester maturity regarding their passive membrane properties but failed to reproduce the action potential threshold and network activity expected in this period. Altogether, our data suggest that passive electrophysiological parameters together with spontaneous activity may serve as useful markers to determine the maturity of iPSC-derived neurons.

Figure 7 (modified from Evrard et al., 1996) summarizes a comparison of the data obtained in this study with those in the literature and shows which periods of prenatal neurodevelopment are best correlated with the EB and NGN2 protocols. The EB protocol covers a much broader developmental range compared with the NGN2 protocol, which only partially correlates with the first 20 weeks after conception and does not include cell multiplication and migration phases. Co-culturing with astrocytes improves viability of NGN2-derived cultures and enables formation of functional synapses but does not reproduce higher network activity seen in EB-derived cultures. Translational disease modeling using the NGN2 protocol should take these limitations into account and restrict research questions appropriately.

In conclusion, we have shown that human iPSC-derived neurons can achieve synchronized activity reminiscent of spindle bursts previously recorded only in rodent brain, and have highlighted the impact of cell growth on neuronal behavior, estimated the maturity of differentiated neurons, and determined developmental restrictions of NGN2-induced iPSC disease modeling.

EXPERIMENTAL PROCEDURES

Generation of iPSCs

Extraction of skin biopsies for the establishment of fibroblasts cultures or hair plucking for generation of keratinocyte cultures and their use in the generation of iPSCs were approved by the Ethics Committee of Medical Faculty and the University Hospital Tuebingen. All donors signed the consent form. Reprogramming was performed according to an adapted protocol from Takahashi et al. (2007), with details described in Supplemental Information.

NGN2-Based Neural Differentiation

We used doxycycline inducible human NGN2 lentiviral expression. iPSCs transduced with NGN2 and rtTA3 lentivirus and selected with puromycin were incubated for 4 h in medium supplemented with

2.5 μg/mL doxycycline and 10 μM Y-27632, followed by dissociation into single cells using Accutase and plating on poly-L-ornithine/laminin-coated coverslips placed in 24-well plates. We plated 80,000 cells per coverslip in NSC medium (Table S3) enriched with 1 μg/mL doxycycline, 10 μM Y-27632, and 10 μM DAPT. On the following day, medium was changed to NSC containing 1 μg/mL doxycycline, 10 μM DAPT, and 10 μM PD 0325901. On days 3–5, we added 2 μM cytarabine to prevent proliferation of untransduced iPSCs, after which medium changed to a 1:1 mixture of NSC and in-house made BrainPhys medium (BrainPhys basal with N2 and NSC21 supplement, Table S3) (Bardy et al., 2015). On day 8, medium was completely changed to BrainPhys and refreshed every 5 days. For the co-cultivations with murine astrocytes, we used the same protocol except that the cells were cultured on preplated astrocytes (see Supplemental Experimental Procedures) and kept for up to 8 weeks.

EB-Based Neural Differentiation

iPSCs cultivated in mTesR1 were manually dissected into large pieces of similar size (diameter 200 μm), which were then transferred into T25 flasks filled with NSC medium containing 10 μM Y-27632 and 10 ng/mL fibroblast growth factor 2 (FGF2) to form EBs. On the following day, we changed medium to the pure NSC. On day 5, we transferred the EBs to Matrigel-coated 6-cm dishes in medium enriched with 1 μM dorsomorphin and 10 μM SB-431542 and let them adhere. We manually picked rosettes and thus selected for pure neuroepithelium on day 14 from the start of the differentiation. The dissected rosettes were transported into a T25 flask containing NSC plus 10 ng/mL FGF2. On day 21, we carefully triturated the NSC preparation into approximately five same-size (diameter 200 μm) pieces and transported them onto coverslips coated with poly-L-ornithine and laminin. For the first day of terminal differentiation we used medium containing NSC and BrainPhys in 1:1 ratio, supplemented with 10 μM Y-27632, 10 ng/mL brain-derived neurotrophic factor, 10 ng/mL glial cell-derived neurotrophic factor, 10 ng/mL insulin-like growth factor 1, 200 μM ascorbic acid, 1 μM cyclic AMP, and 1 μg/mL laminin. On the following day, we switched to full BrainPhys medium containing the same supplements except for Y-27632. From this point the medium was changed once a week and the supplements were not added to the BrainPhys after the first month. The cells were kept in an incubator that was opened only for medium change once a week.

Electrophysiological Recordings

Whole-cell patch-clamp recordings were performed at 22°C using an Axopatch 200B (Molecular Devices, USA) amplifier connected to Digidata 1440A (Molecular Devices) and pClamp10 (Molecular Devices) acquisition software. The cells were clamped at −70 mV. We recorded capacitance, access resistance (inclusive criterion <20 MΩ) and RMP. For the voltage-clamp recordings, sampling rate was 20 kHz and lowpass filter 5 kHz. For investigation of GDEs, we performed a separate class of recordings in EB-derived neurons (acquisition and analysis are described in Supplemental Experimental Procedures).

qRT-PCR

RNA isolation was performed using a Bioline Kit including on-column DNA digestion. The concentration was measured on NanoDrop ND-1000 (Peqlab, Germany). To test silencing of viral transgenes and upregulation of stem cell markers, we used a one step qRT-PCR kit (Bioline, UK) and ΔΔCt method with GAPDH serving as a housekeeping gene (Reinhardt et al., 2013). Procedures for the expression analysis of KCNQ2 transcripts, sodium channel genes, and markers of GABAergic system maturation are described in Supplemental Experimental Procedures.

Electrophysiological Data Analysis

Data analysis was performed using Clampfit (Molecular Devices), Excel (Microsoft, USA), GraphPad Prism 8 (GraphPad, USA) and MATLAB (Mathworks, USA) software. Only cells with RMP < −50 mV and more than one spike in evoked firing protocol were included in the analysis. For evoked firing, only action potentials or spikes with amplitudes reaching 25 mV positive deviation from interspike plateau before the investigated spike were accepted. Action potential threshold was calculated as the voltage of the first derivation value of 20 V/s of the first spike in a 1,000-Hz lowpass filtered trace that had four action potentials in the evoked firing curve.

SUPPLEMENTAL INFORMATION

Supplemental Information can be found online at https://doi.org/10.1016/j.stemcr.2020.05.015.

AUTHOR CONTRIBUTIONS

Conceptualization, F.R.; Methodology, F.R., A.D., H. Loeffler, G.E., and S. Mueller; Software, G.D.C.M.; Investigation: F.R., N.S., B.U., M.C.-L., and C.C.; Writing – Original Draft, F.R., S. Maljevic, and H. Lerche; Writing – Review and Editing, all authors; Resources, H.L., S.P., and P.H.; Funding Acquisition, H. Lerche and S. Maljevic; Supervision, S. Maljevic and H. Lerche.

ACKNOWLEDGMENTS

We thank Drs. Ulrike Hedrich-Klimosch and Henner Koch for their excellent technical help regarding electrophysiological recordings, and Stephan Liebau and the members of his team for their highly appreciated assistance with cultures of keratinocytes. Drs. Olga Garaschuk, Andreas Hermann, Simone Mayer, Ulrike Hedrich-Klimosch, Henner Koch, and Thomas Wuttke are thanked for their helpful comments and discussion of the manuscript. This work was supported by the Federal Ministry of Education and Research (BMBF, grants 01GM1105A and 01GM1907A in the frame of the networks for rare diseases IonNeurONet and TreatION). F.R. was supported by the DAAD program (91529082) and Endeavor Research Fellowship Program (6093_2017). N.S. was in part supported by the Pate/Fortüne program of the Medical Faculty of the University of Tübingen (2381-0-0). The authors declare no competing interests.

Received: June 24, 2019
Revised: May 19, 2020
Accepted: May 20, 2020
Published: June 18, 2020

REFERENCES

Bardy, C., van den Hurk, M., Eames, T., Marchand, C., Hernandez, R.V., Kellogg, M., Gorris, M., Galet, B., Palomares, V., Brown, J., et al. (2015). Neuronal medium that supports basic synaptic functions and activity of human neurons in vitro. Proc. Natl. Acad. Sci. U S A *112*, E2725–E2734.

Bardy, C., van den Hurk, M., Kakaradov, B., Erwin, J.A., Jaeger, B.N., Hernandez, R.V., Eames, T., Paucar, A.A., Gorris, M., Marchand, C., et al. (2016). Predicting the functional states of human iPSC-derived neurons with single-cell RNA-seq and electrophysiology. Mol. Psychiatry *21*, 1573–1588.

Ben-Ari, Y., Cherubini, E., Corradetti, R., and Gaiarsa, J.L. (1989). Giant synaptic potentials in immature rat CA3 hippocampal neurones. J. Physiol. (Lond.) *416*, 303–325.

Bershteyn, M., Nowakowski, T.J., Pollen, A.A., Di Lullo, E., Nene, A., Wynshaw-Boris, A., and Kriegstein, A.R. (2017). Human iPSC-derived cerebral organoids model cellular features of lissencephaly and reveal prolonged mitosis of outer radial glia. Cell Stem Cell *20*, 435–449.e4.

Birey, F., Andersen, J., Makinson, C.D., Islam, S., Wei, W., Huber, N., Fan, H.C., Metzler, K.R.C., Panagiotakos, G., Thom, N., et al. (2017). Assembly of functionally integrated human forebrain spheroids. Nature *545*, 54–59.

Biser, P.S., Thayne, K.A., Kong, J.Q., Fleming, W.W., and Taylor, D.A. (2000). Quantification of the alpha(3) subunit of the Na(+)/K(+)-ATPase in developing rat cerebellum. Brain Res. Dev. Brain Res. *123*, 165–172.

Busskamp, V., Lewis, N.E., Guye, P., Ng, A.H.M., Shipman, S.L., Byrne, S.M., Sanjana, N.E., Murn, J., Li, Y., Li, S., et al. (2014). Rapid neurogenesis through transcriptional activation in human stem cells. Mol. Syst. Biol. *10*, 760.

Chambers, S.M., Fasano, C.A., Papapetrou, E.P., Tomishima, M., Sadelain, M., and Studer, L. (2009). Highly efficient neural conversion of human ES and iPS cells by dual inhibition of SMAD signaling. Nat. Biotechnol. *27*, 275–280.

Connors, B.W., Benardo, L.S., and Prince, D.A. (1983). Coupling between neurons of the developing rat neocortex. J. Neurosci. *3*, 773–782.

Dehay, C., Kennedy, H., and Kosik, K.S. (2015). The outer subventricular zone and primate-specific cortical complexification. Neuron *85*, 683–694.

Dupont, E., Hanganu, I.L., Kilb, W., Hirsch, S., and Luhmann, H.J. (2006). Rapid developmental switch in the mechanisms driving early cortical columnar networks. Nature *439*, 79–83.

Espuny-Camacho, I., Michelsen, K.A., Gall, D., Linaro, D., Hasche, A., Bonnefont, J., Bali, C., Orduz, D., Bilheu, A., Herpoel, A., et al. (2013). Pyramidal neurons derived from human pluripotent stem cells integrate efficiently into mouse brain circuits in vivo. Neuron *77*, 440–456.

Evrard, P., Gadisseux, J.-F., and Gressens, P. (1996). Hypoxia opportunism during brain development. In Acute Perinatal Asphyxia in Term Infants, L.L. Wright, G.B. Merenstein, and D. Hirtz, eds. (Department of Health and Human Services, Public Health Service, National Institutes of Health, National Institute of Child Health and Human Development, NIH Publication No. 96-3823), pp. 43–50, 55–60.

Garaschuk, O., Linn, J., Eilers, J., and Konnerth, A. (2000). Large-scale oscillatory calcium waves in the immature cortex. Nat. Neurosci. *3*, 452–459.

Geschwind, D.H., and Rakic, P. (2013). Cortical evolution: judge the brain by its cover. Neuron *80*, 633–647.

Kadoshima, T., Sakaguchi, H., Nakano, T., Soen, M., Ando, S., Eiraku, M., and Sasai, Y. (2013). Self-organization of axial polarity, inside-out layer pattern, and species-specific progenitor dynamics in human ES cell-derived neocortex. Proc. Natl. Acad. Sci. USA *110*, 20284–20289.

Khirug, S., Huttu, K., Ludwig, A., Smirnov, S., Voipio, J., Rivera, C., Kaila, K., and Khiroug, L. (2005). Distinct properties of functional KCC2 expression in immature mouse hippocampal neurons in culture and in acute slices. Eur. J. Neurosci. *21*, 899–904.

Kirkeby, A., Grealish, S., Wolf, D.A., Nelander, J., Wood, J., Lundblad, M., Lindvall, O., and Parmar, M. (2012). Generation of regionally specified neural progenitors and functional neurons from human embryonic stem cells under defined conditions. Cell Rep. *1*, 703–714.

Kirmse, K., Kummer, M., Kovalchuk, Y., Witte, O.W., Garaschuk, O., and Holthoff, K. (2015). GABA depolarizes immature neurons and inhibits network activity in the neonatal neocortex in vivo. Nat. Commun. *6*, 7750.

Lam, R.S., Töpfer, F.M., Wood, P.G., Busskamp, V., and Bamberg, E. (2017). Functional maturation of human stem cell-derived neurons in long-term cultures. PLoS One *12*, e0169506.

Lancaster, M.A., Renner, M., Martin, C.-A., Wenzel, D., Bicknell, L.S., Hurles, M.E., Homfray, T., Penninger, J.M., Jackson, A.P., and Knoblich, J.A. (2013). Cerebral organoids model human brain development and microcephaly. Nature *501*, 373–379.

Leinekugel, X., Medina, I., Khalilov, I., Ben-Ari, Y., and Khazipov, R. (1997). Ca2+ oscillations mediated by the synergistic excitatory actions of GABA(A) and NMDA receptors in the neonatal hippocampus. Neuron *18*, 243–255.

Liu, Y., Lopez-Santiago, L.F., Yuan, Y., Jones, J.M., Zhang, H., O'Malley, H.A., Patino, G.A., O'Brien, J.E., Rusconi, R., Gupta, A., et al. (2013). Dravet syndrome patient-derived neurons suggest a novel epilepsy mechanism. Ann. Neurol. *74*, 128–139.

Luhmann, H.J., and Khazipov, R. (2018). Neuronal activity patterns in the developing barrel cortex. Neuroscience *368*, 256–267.

Mansour, A.A., Gonçalves, J.T., Bloyd, C.W., Li, H., Fernandes, S., Quang, D., Johnston, S., Parylak, S.L., Jin, X., and Gage, F.H. (2018). An in vivo model of functional and vascularized human brain organoids. Nat. Biotechnol. *36*, 432–441.

Minlebaev, M., Ben-Ari, Y., and Khazipov, R. (2009). NMDA receptors pattern early activity in the developing barrel cortex in vivo. Cereb. Cortex *19*, 688–696.

Moore, A.R., Filipovic, R., Mo, Z., Rasband, M.N., Zecevic, N., and Antic, S.D. (2009). Electrical excitability of early neurons in the human cerebral cortex during the second trimester of gestation. Cereb. Cortex *19*, 1795–1805.

Nehme, R., Zuccaro, E., Ghosh, S.D., Li, C., Sherwood, J.L., Pietilainen, O., Barrett, L.E., Limone, F., Worringer, K.A., Kommineni, S.,

et al. (2018). Combining NGN2 programming with developmental patterning generates human excitatory neurons with NMDAR-mediated synaptic transmission. Cell Rep. *23*, 2509–2523.

Ogiwara, I., Miyamoto, H., Morita, N., Atapour, N., Mazaki, E., Inoue, I., Takeuchi, T., Itohara, S., Yanagawa, Y., Obata, K., et al. (2007). Nav1.1 localizes to axons of parvalbumin-positive inhibitory interneurons: a circuit basis for epileptic seizures in mice carrying an Scn1a gene mutation. J. Neurosci. *27*, 5903–5914.

Pruunsild, P., Bengtson, C.P., and Bading, H. (2017). Networks of cultured iPSC-derived neurons reveal the human synaptic activity-regulated adaptive gene program. Cell Rep. *18*, 122–135.

Qian, X., Nguyen, H.N., Song, M.M., Hadiono, C., Ogden, S.C., Hammack, C., Yao, B., Hamersky, G.R., Jacob, F., Zhong, C., et al. (2016). Brain-region-specific organoids using mini-bioreactors for modeling ZIKV exposure. Cell *165*, 1238–1254.

Quadrato, G., Nguyen, T., Macosko, E.Z., Sherwood, J.L., Min Yang, S., Berger, D.R., Maria, N., Scholvin, J., Goldman, M., Kinney, J.P., et al. (2017). Cell diversity and network dynamics in photosensitive human brain organoids. Nature *545*, 48–53.

Rama, S., Zbili, M., Bialowas, A., Fronzaroli-Molinieres, L., Ankri, N., Carlier, E., Marra, V., and Debanne, D. (2015). Presynaptic hyperpolarization induces a fast analogue modulation of spike-evoked transmission mediated by axonal sodium channels. Nat. Commun. *6*, 10163.

Reinhardt, P., Schmid, B., Burbulla, L.F., Schöndorf, D.C., Wagner, L., Glatza, M., Höing, S., Hargus, G., Heck, S.A., Dhingra, A., et al. (2013). Genetic correction of a LRRK2 mutation in human iPSCs links parkinsonian neurodegeneration to ERK-dependent changes in gene expression. Cell Stem Cell *12*, 354–367.

Rivera, C., Voipio, J., Payne, J.A., Ruusuvuori, E., Lahtinen, H., Lamsa, K., Pirvola, U., Saarma, M., and Kaila, K. (1999). The K^+/Cl^- co-transporter KCC2 renders GABA hyperpolarizing during neuronal maturation. Nature *397*, 251–255.

Royeck, M., Horstmann, M.-T., Remy, S., Reitze, M., Yaari, Y., and Beck, H. (2008). Role of axonal NaV1.6 sodium channels in action potential initiation of CA1 pyramidal neurons. J. Neurophysiol. *100*, 2361–2380.

Rubio, A., Luoni, M., Giannelli, S.G., Radice, I., Iannielli, A., Cancellieri, C., Di Berardino, C., Regalia, G., Lazzari, G., Menegon, A., et al. (2016). Rapid and efficient CRISPR/Cas9 gene inactivation in human neurons during human pluripotent stem cell differentiation and direct reprogramming. Sci. Rep. *6*, 37540.

Rush, A.M., Dib-Hajj, S.D., and Waxman, S.G. (2005). Electrophysiological properties of two axonal sodium channels, Nav1.2 and Nav1.6, expressed in mouse spinal sensory neurones. J. Physiol. (Lond.) *564*, 803–815.

Smith, J.S., Iannotti, C.A., Dargis, P., Christian, E.P., and Aiyar, J. (2001). Differential expression of kcnq2 splice variants: implications to m current function during neuronal development. J. Neurosci. *21*, 1096–1103.

Stein, J.L., de la Torre-Ubieta, L., Tian, Y., Parikshak, N.N., Hernández, I.A., Marchetto, M.C., Baker, D.K., Lu, D., Hinman, C.R., Lowe, J.K., et al. (2014). A quantitative framework to evaluate modeling of cortical development by neural stem cells. Neuron *83*, 69–86.

Sun, Y., Paşca, S.P., Portmann, T., Goold, C., Worringer, K.A., Guan, W., Chan, K.C., Gai, H., Vogt, D., Chen, Y.-J.J., et al. (2016). A deleterious Nav1.1 mutation selectively impairs telencephalic inhibitory neurons derived from Dravet syndrome patients. eLife *5*. https://doi.org/10.7554/eLife.13073.

Tadros, M.A., Farrell, K.E., Graham, B.A., Brichta, A.M., and Callister, R.J. (2015). Properties of sodium currents in neonatal and young adult mouse superficial dorsal horn neurons. Mol. Pain *11*, 17.

Takahashi, K., Tanabe, K., Ohnuki, M., Narita, M., Ichisaka, T., Tomoda, K., and Yamanaka, S. (2007). Induction of pluripotent stem cells from adult human fibroblasts by defined factors. Cell *131*, 861–872.

Testa-Silva, G., Verhoog, M.B., Linaro, D., de Kock, C.P.J., Baayen, J.C., Meredith, R.M., De Zeeuw, C.I., Giugliano, M., and Mansvelder, H.D. (2014). High bandwidth synaptic communication and frequency tracking in human neocortex. PLoS Biol. *12*, e1002007.

Tidball, A.M., and Parent, J.M. (2016). Concise review: exciting cells: modeling genetic epilepsies with patient-derived induced pluripotent stem cells. Stem Cells *34*, 27–33.

Trujillo, C.A., Gao, R., Negraes, P.D., Gu, J., Buchanan, J., Preissl, S., Wang, A., Wu, W., Haddad, G.G., Chaim, I.A., Domissy, A., Vandenberghe, M., Devor, A., Yeo, G.W., Voytek, B., and Muotri, A.R. (2019). Complex oscillatory waves emerging from cortical organoids model early human brain network development. Cell Stem Cell *25*, 558–569.

Valiullina, F., Akhmetshina, D., Nasretdinov, A., Mukhtarov, M., Valeeva, G., Khazipov, R., and Rozov, A. (2016). Developmental changes in electrophysiological properties and a transition from electrical to chemical coupling between excitatory layer 4 neurons in the rat barrel cortex. Front. Neural Circuits *10*, 1.

Vanhatalo, S., and Kaila, K. (2006). Development of neonatal EEG activity: from phenomenology to physiology. Semin. Fetal Neonatal. Med. *11*, 471–478.

Vanhatalo, S., Tallgren, P., Andersson, S., Sainio, K., Voipio, J., and Kaila, K. (2002). DC-EEG discloses prominent, very slow activity patterns during sleep in preterm infants. Clin. Neurophysiol. *113*, 1822–1825.

Watari, H., Tose, A.J., and Bosma, M.M. (2013). Hyperpolarization of resting membrane potential causes retraction of spontaneous $Ca(i)^{2+}$ transients during mouse embryonic circuit development. J. Physiol. (Lond.) *591*, 973–983.

Yu, Y.-C., He, S., Chen, S., Fu, Y., Brown, K.N., Yao, X.-H., Ma, J., Gao, K.P., Sosinsky, G.E., Huang, K., et al. (2012). Preferential electrical coupling regulates neocortical lineage-dependent microcircuit assembly. Nature *486*, 113–117.

Yu, F.H., Mantegazza, M., Westenbroek, R.E., Robbins, C.A., Kalume, F., Burton, K.A., Spain, W.J., McKnight, G.S., Scheuer, T., and Catterall, W.A. (2006). Reduced sodium current in GABAergic interneurons in a mouse model of severe myoclonic epilepsy in infancy. Nat. Neurosci. *9*, 1142–1149.

Yuan, F., Fang, K.-H., Cao, S.-Y., Qu, Z.-Y., Li, Q., Krencik, R., Xu, M., Bhattacharyya, A., Su, Y.-W., Zhu, D.-Y., et al. (2015). Efficient

generation of region-specific forebrain neurons from human pluripotent stem cells under highly defined condition. Sci. Rep. *5*, 18550.

Zhang, S.C., Wernig, M., Duncan, I.D., Brüstle, O., and Thomson, J.A. (2001). In vitro differentiation of transplantable neural precursors from human embryonic stem cells. Nat. Biotechnol. *19*, 1129–1133.

Zhang, Y., Pak, C., Han, Y., Ahlenius, H., Zhang, Z., Chanda, S., Marro, S., Patzke, C., Acuna, C., Covy, J., et al. (2013). Rapid single-step induction of functional neurons from human pluripotent stem cells. Neuron *78*, 785–798.

Zhong, P., Hu, Z., Jiang, H., Yan, Z., and Feng, J. (2017). Dopamine induces oscillatory activities in human midbrain neurons with parkin mutations. Cell Rep. *19*, 1033–1044.